Journal of *Marine Science and Engineering*

MDPI

*Article*

# Performance of Oil Spill Identification in Multiple Scenarios Using Quad-, Compact-, and Dual-Polarization Modes

**Guannan Li [1], Gaohuan Lv [1], Bingnan Li [2], Xiang Wang [3] and Fen Zhao [4,*]**

[1] Ulsan Ship and Ocean College, Ludong University, Yantai 264025, China; liguannan@ldu.edu.cn (G.L.); lvgh@ldu.edu.cn (G.L.)
[2] Civil and Environmental Engineering, University of New South Wales, Sydney, NSW 2052, Australia; bingnan.li@unsw.edu.au
[3] Ocean Remote Sensing Division, National Marine Environmental Monitoring Center, Dalian 116026, China; xwang@nmemc.org.cn
[4] School of Resources and Environmental Engineering, Ludong University, Yantai 264025, China
* Correspondence: zhaof@ldu.edu.cn; Tel.: +86-0535-6608369

## Abstract

Oil spills, whether in open water or near shorelines, cause serious environmental problems. Moreover, polarimetric synthetic-aperture radar provides abundant oil spill information with all-weather, day–night detection capability, but its use is limited by data usage and processing costs. Compact Polarimetric (CP) systems as a subsequent emerging system, which balance data volume and system design requirements, are promising in this regard. Herein, we utilize multisource oil spill scenarios and datasets from multiple polarimetric modes (VV-HH, $\pi/4$, DCP, and CTLR) to assess the oil spill detection capability of each mode under varying incidence angles conditions, spill causes, and oil types. Using qualitative and quantitative evaluation indicators, we compare the typical features of the multiple polarization modes as well as assess their consistency with Full Polarization (FP) information and their oil spill recognition performance across different incidence angles. In large-incidence-angle oil spill scenarios, the VV–HH mode exhibits the highest information consistency with the FP mode and the strongest oil spill recognition ability. At small incidence angles, the CP mode (i.e., CTLR mode) exhibits the best overall performance, benefiting from its effective self-calibration capability and low noise sensitivity. Furthermore, despite containing comprehensive information, the FP mode is not always superior to the dual-polarization and CP modes. Thus, in oil spill scenarios across different incidence angles, incorporating features from an appropriate polarization mode into oil spill information extraction and recognition can optimize the associated efficiency.

**Keywords:** oil spill detection; polarimetric synthetic-aperture radar; polarimetric feature; incidence angles

Check for updates

Academic Editor: Weicheng Cui

Received: 25 November 2025
Revised: 20 December 2025
Accepted: 24 December 2025
Published: 6 January 2026

**Copyright:** © 2026 by the authors. Licensee MDPI, Basel, Switzerland. This article is an open access article distributed under the terms and conditions of the Creative Commons Attribution (CC BY) license.

## 1. Introduction

Oil spill pollution affects the marine ecological environment, economic development, and species habitats, as well as associated human activities [1–5]. Therefore, effective detection of marine oil spills can assist in controlling marine oil spill pollution, supporting related decision-making processes, managing marine ecological disasters, and predicting marine pollution disasters. Reducing the negative impacts of oil spill pollution on the abovementioned domains requires promptly and effectively identifying the locations and scopes of oil spills and performing cleanup. Remote sensing can effectively monitor marine

oil spills in the spatial domain, obtain an overview of the oil spill range, perform continuous time-series tracking, and overcome the limitations of traditional monitoring methods [2,4,6]. The use of polarimetric synthetic-aperture radar (PolSAR) to monitor marine oil spills and describe their characteristics has recently become increasingly common.

Full-Polarization (FP) systems can obtain sufficient scattering information for each resolved image pixel, generating images containing amplitude and phase information [5,7]. FP system images provide more physically reliable, comprehensive, and robust results in identification, classification, and other value-added analyses compared with images from Single-Polarization or Dual-Polarization (DP) synthetic-aperture radar (SAR). Although the unique advantages of FP SAR systems are crucial for remote sensing-based monitoring, these systems are limited by their pulse repetition rate (twice that of single-polarization or DP systems), which restricts the bandwidth and the range of incidence angles. In addition, the balance of various technologies should be considered, such as antenna design, system energy consumption, data storage, and processing capacity [8–10]. DP systems serve as a bridge connecting single-polarization and FP systems. Although they compromise some polarimetric information richness, they are advantageous in terms of operating costs, complexity, observation range scale, and data storage and processing requirements. Subsequently, Compact Polarimetric (CP) systems have been proposed and are increasingly used in Earth observation applications to meet detection requirements. The construction concept of these systems involves transmitting a polarization mode and performing coherent processing during reception, effectively avoiding the shortcomings of FP systems. They can be regarded as special DP systems that provide richer polarization information than conventional DP modes, including the $\pi/4$, DCP, and CTLR modes [9–12]. However, owing to differences in system architecture, definitions, and information richness between various DP and simplified polarization systems, they exhibit different recognition advantages in different target detection applications. Many studies have been conducted to compare DP/CP with FP structures to investigate the information consistency of identified features; some studies have focused on analyzing and comparing the similarity degree of target features between different DP/CP and FP systems to determine their information consistency and then identify the best solution in the absence of the FP mode [13,14]. Scholars have also conducted comparative studies on the performance of different DP and FP systems in various Earth observation applications to explore the potential and advantages of DP/CP in identifying different targets [15]. The VV–HH mode is advantageous in various target classification applications [16,17]. CP modes are widely employed in Earth observation and exhibit good potential for use in feature extraction and optimization as well as target recognition [18–21]. Hou compared the classification performance of FP, traditional DP, and CP systems based on a unified framework; in different classification tasks, CP systems performed better in agricultural scenarios, whereas traditional DP systems performed better in urban scenarios [22].

DP and CP modes also demonstrate considerable potential and advantages in marine detection, especially in oil spill and ship detections [23,24]. Buono compared two CP modes—the $\pi/4$ and hybrid-polarity modes—based on FP SAR oil spill data simulation; the results showed that the $\pi/4$ mode more closely resembled the FP structure, further verifying the potential of using this CP mode for marine oil spill monitoring [25]. Researchers have studied marine oil spill monitoring based on CP modes, verifying their ability to detect oil spills and similar weak-damping phenomena as well as proving that the oil spill monitoring performance of CP modes is the same as that of traditional measurement methods in terms of polarimetric entropy estimation [26,27]. Given the potential of CP modes in oil spill detection, researchers have reconstructed FP data based on CP modes and explored the consistency of information richness between the reconstructed data and original FP

mode data, demonstrating good consistency in co- and cross-polarization under different observation conditions [28]. However, previous studies have mostly focused on comparing the oil spill information recognition performance and reconstruction information of CP modes with those of the FP mode for single oil spill scenarios. Furthermore, previous studies have primarily conducted information consistency tests based on DP and FP modes, lacking diversity in oil spill scenarios and failing to conduct a comprehensive comparison of traditional FP/DP and CP modes in multisource oil spill scenarios. Moreover, varying oil spill application scenarios and observation conditions can affect target feature expression, and few studies have analyzed how changes in incidence angle affect the information differences among oil spill scenarios across different polarization modes.

The framework and background of this study are inspired by (i) the abovementioned limitations of the literature and other published studies on comparisons of the typical features of oil spills under FP and DP/CP models and (ii) research achievements on the identification of oil spill information. Compared with previous studies, this research contributes two main objectives:

1. Analyze the differences in signal-to-noise levels in various oil spill scenarios at different incidence angles. Compare the relative position distributions of each target and the noise-equivalent sigma zero (NESZ) baseline under the corresponding conditions.

2. Combine the effect of signal-to-noise levels differences at various incidence angles for multiple oil spill scenarios. Perform qualitative comparison and exploration between different features and scattering characteristics at large and small incidence angles.

Although this study is based on limited datasets for comparison and analysis, different results may occur in other experimental scenarios. This research also provides references and guidance for payload system design in marine detection, especially oil spill detection, and for the selection of multiple polarization SAR modes. The aim is the optimal selection of advantageous modes corresponding to different conditions and scenarios.

## 2. Experimental Design and Dataset Overview

The compared traditional DP (VV–HH) and CP ($\pi/4$, DCP, and CTLR) data were simulated from FP data as real multimode data cannot be simultaneously obtained. Various oil spill sites were considered to diversify the analyzed dataset of oil spill scenarios under different incidence angles. It should be noted that the data were qualitatively selected for typical oil spill scenarios with relatively large/small incident angles for validate and summarize the general results, laying the foundation for more continuous analysis in the future. Table 1 presents the dataset information of PolSAR images under different oil spill conditions. The flowchart is shown in Figure 1.

**Table 1.** Properties and descriptions of four sites and imaging information in this study.

| Parameter/Case | Large Incidence Angle | | Small Incidence Angle | |
|---|---|---|---|---|
| | Scene 1 | Scene 2 | Scene 3 | Scene 4 |
| Test Site | Gulf of Mexico | The North Sea Norway | The North Sea Norway | Mississippi River Delta |
| Date | 8 May 2010 | 8 June 2011 | 8 June 2011 | 8 May2015 |
| Time (UTC) | 12:01 | 05:59 | 17:27 | 11:48 |
| Mode/product | Fine/SLC | Fine/SLC | Fine/SLC | Fine/SLC |
| Incidence angle | 41.9°~43.4° | 46.1°~47.3° | 34.5°~36.1° | 26.09°~29.39° |
| Slick present | natural oil seeps | Emulsion/plant | Crude/Emulsion/plant | Nearshore oil |

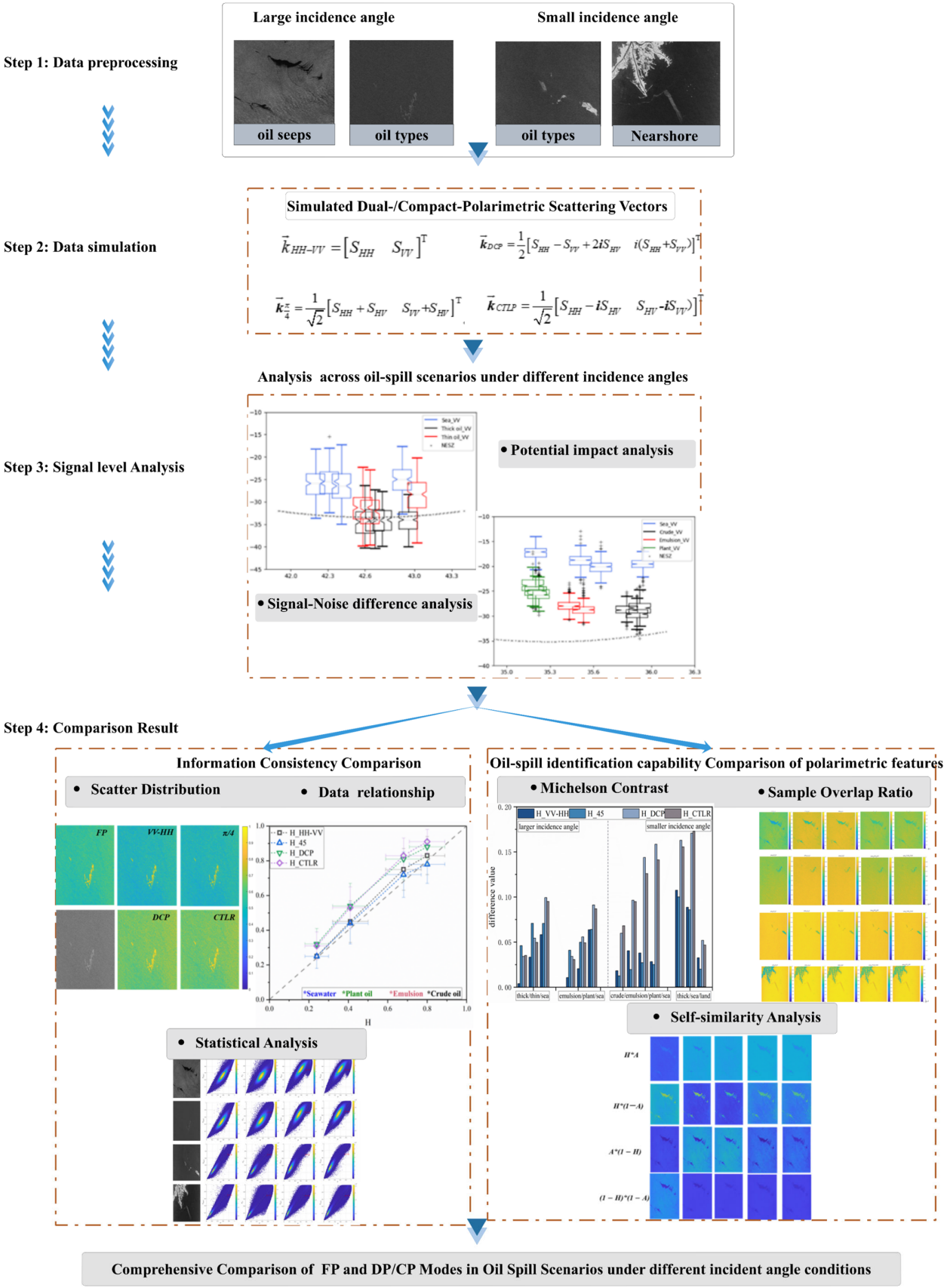



**Figure 1.** Schematic of the overall workflow.

### 2.1. Oil Spill Scenario 1: Natural Oil Seepage

Scenario 1 comprised RADARSAT-2 data corresponding to an obvious dark area interpreted as natural oil seepage in the Gulf of Mexico [5,8]. The imaging time was 12:01 UTC on 8 May 2010. The incidence angle range was 41.9° (near)–43.4° (far). Analytical experiments and studies have shown that this oil slick formed a relatively thick area on the leeward side under the action of wind, and a thin "plume" slick on the windward side [5,8,29]. In subsequent quantitative comparisons, thick oil samples were extracted from the leeward side and thin samples were from the windward side to analyze how the signal varies with oil slick thickness under different polarimetric modes, as shown in Figure 2.



(**a**) (**b**) (**c**) (**d**)

**Figure 2.** Overview of SAR images of experimental area: (**a**) natural oil seepage (large incidence angle), (**b**) different types of oil slick (large incidence angle), (**c**) different types of oil slick (small incidence angle), and (**d**) nearshore oil spill (small incidence angle). All satellite maps were produced using RADARSAT-2 data (intensity images; $\sigma_0$V V [dB]).

### 2.2. Oil Spill Scenario 2: Different Types of Oil Slick (Large Incidence Angle)

The Norwegian Clean Seas Association for Operating Companies (NOFO) conducted a manufactured oil-on-water experiment in the North Sea from 6 June 2011, to 9 June 2011, to explore the scattering mechanisms and characteristic differences between various types of oil slick. Two sets of RADARSAT-2 image data were obtained in the experiment, which the details of the composition and characteristics of the oil slick provided in [4]; their imaging times were 5:59 UTC on 7 June 2011, and 17:27 UTC on 8 June 2011. The 5:59 UTC image showed plant oil and emulsion, released ~2 and ~18 h, respectively, before satellite passage. The incidence angle of the image ranged from 46.1° (near) to 47.3° (far)—the larger incidence angle between the two images obtained in this experiment [4].

### 2.3. Oil Spill Scenario 3: Different Types of Oil Slick (Small Incidence Angle)

The abovementioned 17:27 UTC (8 June 2011) RADARSAT-2 image shows three types of oil slick: (left to right) plant oil, emulsion, and crude oil. They were present for 13, 29, and 9 h, respectively, before satellite passage, and the time interval with Scenario 2 is 12 h [4]. The incidence angle range of the image is 34.5° (near) to 36.1° (far), which is smaller compared with that in Scenario 2. The data of Scenarios 2 and 3 were from the same sea area and the same oil spill scenario, enabling comparisons at different incidence angles observation conditions.

### 2.4. Oil Spill Scenario 4: Nearshore Oil Spill Incidence

The image selected for Scenario 4 was from an oil spill accident in the nearshore waters of the Mississippi River Delta. The imaging time was 23:53 UTC on 8 May 2015. This image, containing targets such as oil spills, land, and seawater, has been used and interpreted in other studies. Its incidence angle range is 26° (near)–29.3° (far)—a small incidence angle among the four oil spill images in these scenarios [30].

## 3. Method

### 3.1. Structure from Multi-Polarization-Mode Data

#### 3.1.1. FP SAR System and Theoretical Structure

The FP system transmits and receives polarization channels in four linear combinations. Owing to their ability to acquire abundant information of targets, such systems have been widely used in various oil spill scenarios. For the matrix of a pure (single) target, the subscripts $x$ and $y$ of matrix element $S_{xy}$ represent the transmitted and received polarizations, respectively, with $x, y \in \{H,V\}$. The scattering matrix $S$ and scattering vectors defined in the FP system are as follows [7,25]:

$$S = \begin{bmatrix} S_{HH} & S_{VH} \\ S_{HV} & S_{VV} \end{bmatrix} = \begin{bmatrix} |S_{HH}|e^{i\boldsymbol{\Phi}HH} & |S_{HV}|e^{i\boldsymbol{\Phi}VH} \\ |S_{VH}|e^{i\boldsymbol{\Phi}HV} & |S_{VV}|e^{i\boldsymbol{\Phi}VV} \end{bmatrix} \quad (1)$$

where $\Phi_{ij}$ and $|\bullet|$ represent the measured phase and amplitude information, respectively. Assuming reciprocity (i.e., $S_{HV} = S_{VH}$), the corresponding three-dimensional lexicographic scattering vector $\vec{k}_{FP}$ is as follows [7]:

$$\vec{\boldsymbol{k}}_{FP} = \begin{bmatrix} S_{HH} & \sqrt{2}S_{VH} & S_{VV} \end{bmatrix}^{\mathrm{T}} \quad (2)$$

The $3 \times 3$ multilook covariance matrix $C_3$ is defined based on the outer product of $k_{FP}$ and its conjugate transpose $k_{FP}^{*T}$.

$$\langle C \rangle_{FP} = < k_{FP} \cdot k_{FP}^{*T} > = \begin{bmatrix} \left\langle |S_{HH}|^2 \right\rangle & \sqrt{2}\langle S_{HH}S_{HV}^* \rangle & \langle S_{HH}S_{VV}^* \rangle \\ \sqrt{2}\langle S_{HV}S_{HH}^* \rangle & 2\left\langle |S_{HV}|^2 \right\rangle & \sqrt{2}\langle S_{HV}S_{VV}^* \rangle \\ \langle S_{VV}S_{HH}^* \rangle & \sqrt{2}\langle S_{VV}S_{HV}^* \rangle & \left\langle |S_{VV}|^2 \right\rangle \end{bmatrix} \quad (3)$$

where $< >$ denotes ensemble averaging.

#### 3.1.2. Structure from DP/CP Data

The DP/CP data used in this study were derived from FP system simulations due to the impossibility of concurrently obtaining multisource oil spill images under different polarization modes. The scattering vectors and corresponding covariance matrices defined by the DP/CP modes (VV–HH, $\pi/4$, DCP, and CTLR) are presented in Table 2 [9–11].

**Table 2.** Comparison of DP scattering vectors and corresponding covariance matrix.

| DP/CP Scattering Vector | Corresponding Covariance Matrix |
| --- | --- |
| $\vec{k}_{HH-VV} = \begin{bmatrix} S_{HH} & S_{VV} \end{bmatrix}^{\mathrm{T}}$ | $\langle C \rangle_{VV-HH} = \begin{bmatrix} \left\langle \lvert S_{VV} \rvert^2 \right\rangle & \langle S_{VV}S_{VH}^* \rangle \\ \langle S_{VH}S_{VV}^* \rangle & \left\langle \lvert S_{HH} \rvert^2 \right\rangle \end{bmatrix}$ |
| $\vec{k}_{\frac{\pi}{4}} = \frac{1}{\sqrt{2}}\begin{bmatrix} S_{HH}+S_{HV} & S_{VV}+S_{HV} \end{bmatrix}^{\mathrm{T}}$ | $\langle C \rangle_{\frac{\pi}{4}} = \frac{1}{2}\begin{bmatrix} \left\langle \lvert S_{HH}+S_{HV} \rvert^2 \right\rangle & \langle (S_{HH}+S_{HV})(S_{VV}+S_{HV})^* \rangle \\ \langle (S_{VV}+S_{HV})(S_{HH}+S_{HV})^* \rangle & \left\langle \lvert S_{VV}+S_{VH} \rvert^2 \right\rangle \end{bmatrix}$ |
| $\vec{k}_{DCP} = \frac{1}{2}\begin{bmatrix} S_{HH}-S_{VV}+2iS_{HV} & i(S_{HH}+S_{VV}) \end{bmatrix}^{\mathrm{T}}$ | $\langle C \rangle_{DCP} = \frac{1}{4}\begin{bmatrix} \left\langle \lvert S_{HH}-S_{VV}+2iS_{HV} \rvert^2 \right\rangle & \langle -i(S_{HH}-S_{VV}+2iS_{HV})(S_{HH}+S_{VV})^* \rangle \\ \langle i(S_{HH}+S_{VV})(S_{HH}-S_{VV}+2iS_{HV})^* \rangle & \left\langle \lvert S_{HH}+S_{VV} \rvert^2 \right\rangle \end{bmatrix}$ |
| $\vec{k}_{CTLP} = \frac{1}{\sqrt{2}}\begin{bmatrix} S_{HH}-iS_{HV} & S_{HV}-iS_{VV}) \end{bmatrix}^{\mathrm{T}}$ | $\langle C \rangle_{CTLR} = \frac{1}{2}\begin{bmatrix} \left\langle \lvert S_{HH}-iS_{HV} \rvert^2 \right\rangle & \langle (S_{HH}-iS_{HV})(S_{HV}-iS_{VV})^* \rangle \\ \langle (S_{HV}-iS_{VV})(S_{HH}-iS_{VV})^* \rangle & \left\langle \lvert S_{HV}-iS_{VV} \rvert^2 \right\rangle \end{bmatrix}$ |

### 3.2. Noise Analysis

The radar scattering signals of ground objects are usually regarded as only returning a portion of the total power of the incident radar [4]. In this case, the NESZ is the equivalent

value of an instrument's background noise and represents the scattering signal detection benchmark for normalized radar cross section (NRCS) data of the signal level, which is an effective, important tool for measuring and analyzing the signal levels of ground objects. To some extent, the NESZ can be used to evaluate the influence of the equivalent noise of the system on the ability to recognize oil spills in SAR images [31]. Therefore, the signal levels of oil spills and ambient signals should be comprehensively compared to analyze the differences in signal levels across oil spill scenarios under varying polarimetric channels. Furthermore, the relative distributions of various oil spill target signals should be compared with the NESZ baseline at different incidence angles, and the degree of influence of satellite background noise on these signal levels should be examined. This approach is also an important reference indicator for subsequent comparisons of similarity between scattering mechanisms and typical feature parameters with multiple polarimetric modes.

### *3.3. Extraction of Typical Polarimetric Features for Multi-Polarization Modes*

The differences in multiple polarization modes and the information consistency across oil spill scenarios at various incidence angles are quantitatively determined in this study using polarimetric features that are widely used in oil spill identification research for extraction and comparison. These features have been applied to and proven effective for the FP data used in this study [4,5,8,29]. On this basis, this research further expands the application of these typical features to the DP/CP mode and evaluates oil spill information extraction capabilities under different polarization modes in various data scenarios.

#### 3.3.1. Polarimetric Scattering Entropy

Polarimetric scattering entropy $H$ represents the degree of randomness of the main dominant scattering mechanism in the target area, reflecting its depolarization degree to some extent. Therefore, it is widely used to identify oil spill information [1,4,8] and has gradually expanded to various combinations of polarimetric features. It is defined as follows:

$$H = -\sum_{i=1}^{N} P_i \log_N P_i \tag{4}$$

$$P_i = \frac{\lambda_i}{\sum_{i=1}^{N} \lambda_i} \tag{5}$$

where $\lambda_i$ are the eigenvalues of the coherent matrix, and $N$ is the polarization dimension used in the FP, DP, and CP modes.

#### 3.3.2. H_A Combination Features

Given the discrimination capabilities of comprehensive polarimetric scattering entropy $H$ and anisotropy $A$ for oil slick and seawater and considering the expansion ability of this combination, this paper uses the $H_A$ combination parameter, which has been widely used in oil spill detection [21,32], for subsequent comparison and analysis.

$$H_A = \begin{cases} HA \\ H(1-A) \\ A(1-H) \\ (1-H)(1-A) \end{cases} \tag{6}$$

$H$ represents the polarimetric scattering entropy under the corresponding polarization mode (Section 3.3.1) and $A$ represents polarimetric anisotropy. Supplementing $H$, $A$ describes the relative magnitudes of the eigenvalues, and its definition is as follows [7]:

$$A = \frac{\lambda_{\max} - \lambda_{\min}}{\lambda_{\max} + \lambda_{\min}} \tag{7}$$

#### 3.3.3. Randomness of Target Scattering

The self-similarity parameter ($rrr_s$) is derived from the random scattering similarity parameter ($rrr$) under the corresponding relationship of a mixed scatterer $T$ and a canonical mixed scatterer $Tc$ where $T = cTc$, where $c$ is an arbitrary complex number, as initially defined by [33]. To a certain extent, the self-similarity parameter expresses the complexity and randomness of the target scattering mechanism, which is suitable for the detection and extraction of oil spills. Its effective use in detecting and identifying oil spills and effectively extracting mineral and plant oils has been verified [34]. Its definition is as follows:

$$rrr_s(T, T_C) = \frac{\sum_{i=1}^{N} \lambda_i \lambda_{ci}}{\sum_{i=1}^{N} \lambda_i \sum_{i=1}^{N} \lambda_{ci}} = \frac{\sum_{i=1}^{N} \lambda_i^2}{\left(\sum_{i=1}^{N} \lambda_i\right)^2} = \frac{tr(TT^H)}{(tr(T))^2} \tag{8}$$

The range of "$rrr_s$" is [1/3, 1]. The simpler the target scattering mechanism, the larger the target self-similarity value. These two extreme values correspond to an equivalent point scatterer with a single target position and pure random noise.

### *3.4. Evaluation Indicators for Identification Capability of Typical Polarimetric Features*

Assessment of the information extraction capability of polarimetric features for oil spill targets mainly involves two aspects: the separation and confusion degrees between target samples. In this research, the Michelson Contrast (MC) and Overlap Ratio (OR) are used to conduct pairwise measurements in the one-dimensional polarimetric feature space.

#### 3.4.1. Michelson Contrast

Selecting dominant features by evaluating regional contrasts is a key point in identifying oil spill targets. The MC is widely used in contrast measurements of oil slick and background information and has become a general indicator in oil target recognition and classification [4,35]. It was initially used to compare target pairs in images. In this paper, it is used to identify differences in parameters between the FP and DP/CP modes. The MC is defined as follows:

$$\boldsymbol{MC} = \frac{|I_i - I_j|}{I_i + I_j} \tag{9}$$

where $I_i$ and $I_j$ are the statistical averages of the one-dimensional feature parameter between two different region samples being compared. According to this definition, the MC value is in the range [0, 1]. In this paper, the MC is mainly evaluated in the following two ways:

(1) For assessing the information consistency of the DP/CP mode with the FP mode, $I_i$ denotes the DP/CP mode, and $I_j$ denotes the FP mode. The MC measure is used to assess the feature difference between the DP/CP and FP modes. The smaller the result, the higher the degree of information consistency, and vice versa.

(2) For distinguishing between oil spill targets and background information within a single polarimetric feature space, $I_i$ and $I_j$ represent different region samples in the one-dimensional feature parameter. Hence, the MC measure reflects the degree of difference

between the targets under this feature to extract oil spill information. The larger the result, the greater the inter-class difference.

#### 3.4.2. Overlap Ratio

We extract and count the overlapping samples between targets in the one-dimensional feature, obtain their proportions relative to the total samples [29], and define the result as follows:

$$\boldsymbol{OR} = \frac{\boldsymbol{m}_{i\&j}}{\boldsymbol{m}_{\boldsymbol{total}}} \tag{10}$$

where $\boldsymbol{m}_{i\&j}$ and $\boldsymbol{m}_{total}$ are the number of overlapping samples between the two targets and the total number of samples in the considered dataset, respectively. In this study, the sample quantities used for pairwise comparisons under the same evaluation criteria are calculated by selecting the same number of adjacent samples for comparison.

## 4. Results and Analysis

### *4.1. NESZ Analysis*

The target signal levels in the considered oil spill scenarios are compared with the background noise and plotted according to the corresponding incidence angle relationship, as shown in the Figure 3. Overall, the VV channel exhibits the highest signal values; in addition, the backscatter decreases faster in the HH channel than in the VV channel, consistent with the hypothesis [4]. The cross-polarization channel (VH) exhibits the lowest signal intensity; approximately 75% of the data are below the noise baseline, and the samples differ little except in the land target area. With regard to sample distributions, regardless of the oil spill scenario, mineral oil generally exhibits lower signal values than plant oil and thicker oil slicks exhibit lower signal values. In Scenarios 1 and 2, approximately 50% of the oil slick samples in the VV channel are below the NESZ baseline, the seawater samples are contaminated by instrument noise to a certain degree, and the amounts of data below the NESZ baseline in the HH and VH channels gradually increase. In Scenarios 3 and 4, although the HH channel data are generally 2.3–5 dB lower than the VV channel data, the samples are above the NESZ and less affected by the background noise baseline.

For other modes, the data modes are derived from FP data simulation, the scattering vector is obtained through a linear combination of FP data. Taking CTRL as a reference,

(1) Each channel (VV/HH/VH/HV) in the FP system will be transmitted to the corresponding simulation channel through the corresponding combination transformation.

$$E_H = \frac{1}{\sqrt{2}}(S_{HH} - \boldsymbol{i}S_{HV}) \tag{11}$$

$$E_V = \frac{1}{\sqrt{2}}(S_{HV} - \boldsymbol{i}S_{VV}) \tag{12}$$

(2) Based on the linear transformation, derive the relationship between the noise power of the simulation CP channel and that of the FP channel.

However, it should be noted that the magnitude of NESZ is affected by multiple factors, such as system temperature, antenna configuration parameters (e.g., power and gain), and system power consumption [4,31]. During the process of new channel simulations by combining these channels for CP mode, the noise characteristics may also change, not merely being the direct addition result of the noise of each channel. In conclusion, the signal level of the co-polarization channels (VV or HH) is generally higher than that of the VH channel. In addition, images with small incidence angles have higher signal-to-noise ratios and are less affected by the noise than images with large incidence angles. Various

targets in images with larger incidence angles are more affected by the NESZ baseline, with an enlarged proportion of target signals below the baseline.

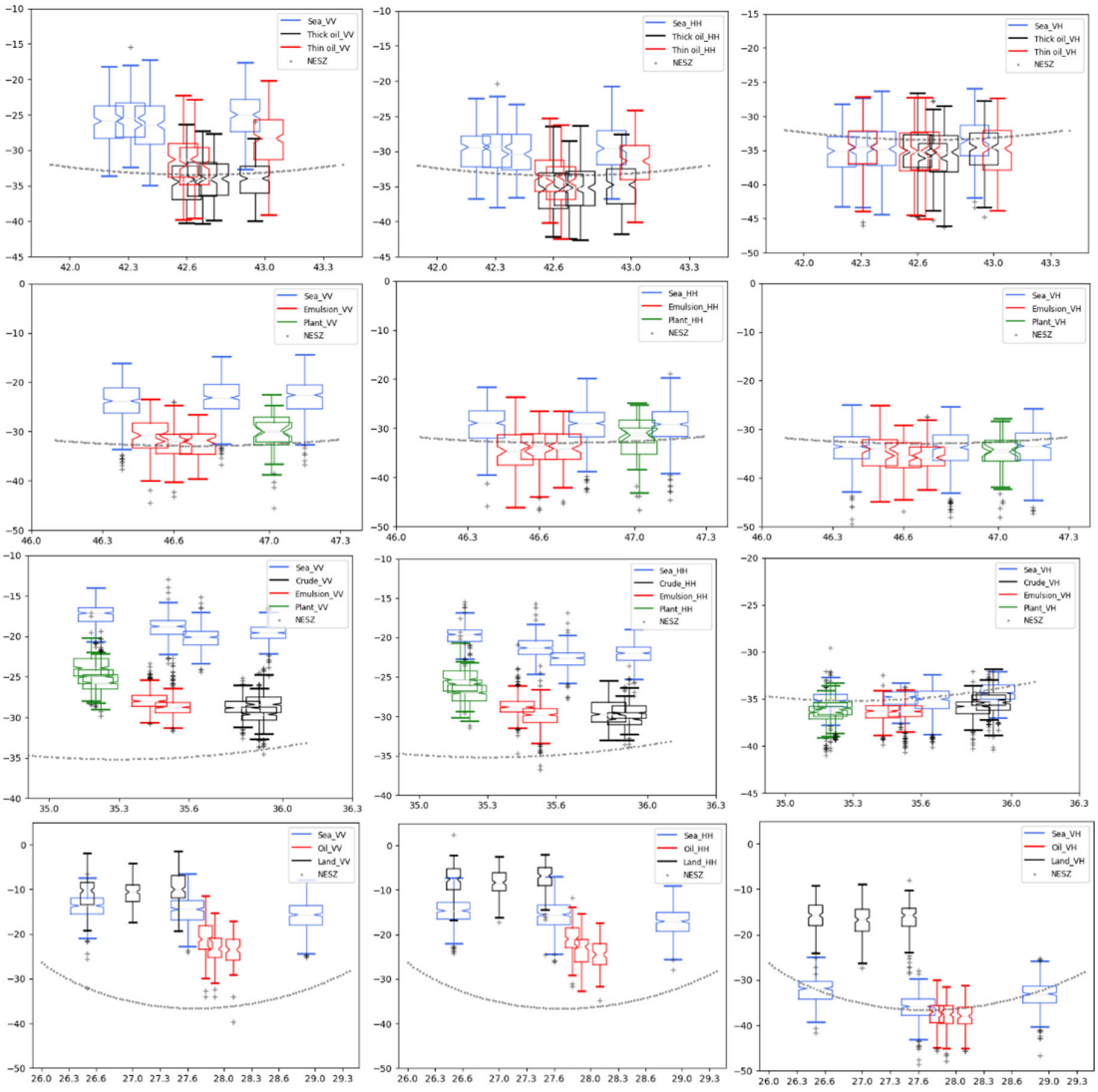



**Figure 3.** Signal-to-noise analyses. From left to right, each column represents VV, HH, and VH channels. Each row represents the oil spill scenarios: different types of oil slick (large incidence angle), different types of oil slick (small incidence angle), natural oil seepage, and nearshore oil spill.

### *4.2. Information Consistency Between DP/CP and FP Modes Under Typical Polarimetric Features*

Polarimetric scattering entropy is a frequently used, universally applicable polarimetric feature in numerous applications, such as target scattering characteristic description, land classification, change detection, and target recognition. Its initial definition was based on FP data, especially in studies on marine oil spill detection, and then gradually expanded to the DP mode. Given the advantages of polarimetric scattering entropy in reflecting the depolarization statistical characteristics of marine targets, given $H$ as the reference, this paper compares polarimetric scattering entropy between DP and CP systems and examines their information consistency with FP. Corresponding to the different polarimetric modes in the research area (Figure 2), the scattering entropy in Figure 4a–d represents the five modes (FP, VVHH, $\pi/4$, DCP, and CTLR modes) in the four scenarios. Overall, the FP and DP/CP modes have similar physical significance. Therefore, regions with high randomness, such as oil slicks and land, show higher entropy values, whereas areas involving a single scattering mechanism on the sea surface show smaller values. A visual comparison

shows that Scenarios 1 and 2 have higher entropy values for both oil spills and seawater dominated by single scattering. The overall lower entropy values of seawater in Scenarios 3 and 4 may be because the seawater samples in the high-incidence-angle images are affected by background noise, which increases randomness and complexity. This conclusion is consistent with relevant research [4,8].

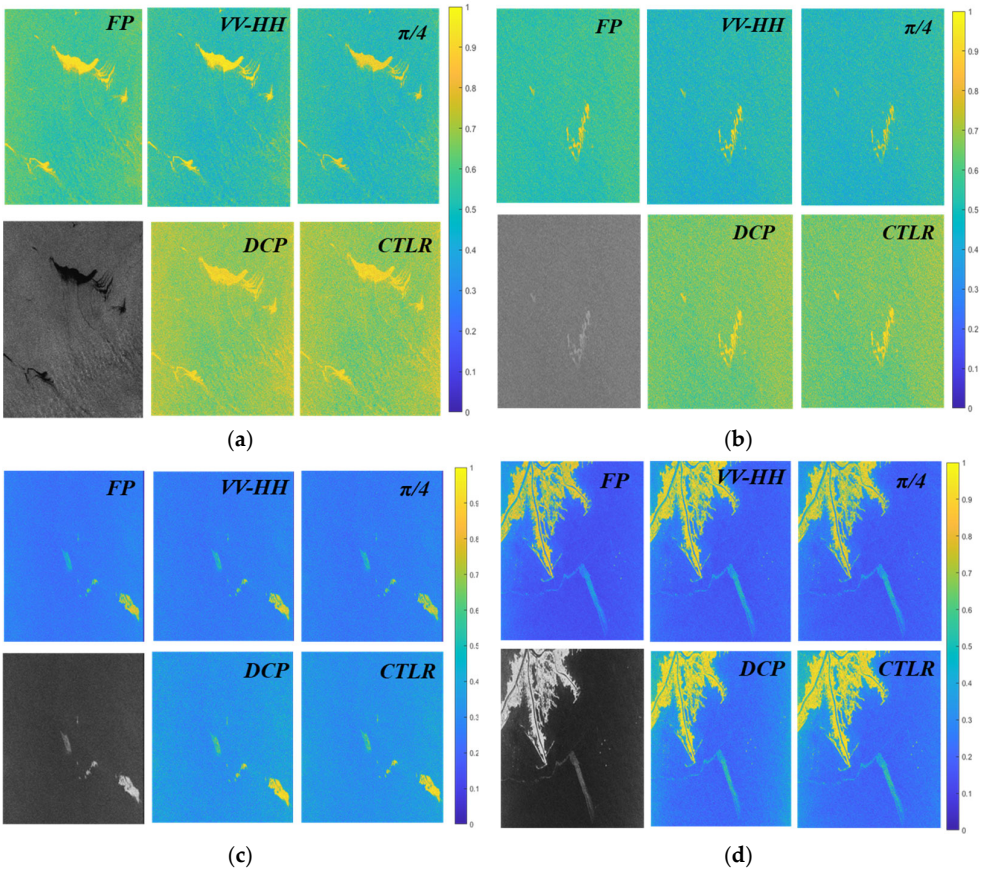



**Figure 4.** Visualization of polarimetric entropy $H$ between FP and DP/CP systems in various oil spill scenarios: (**a**) oil seepage, (**b**) different types of oil slick (large incidence angle), (**c**) different types of oil slick (small incidence angle), (**d**) nearshore oil spill.

The information consistency results for the DP/CP and FP are shown in the Figures 5 and 6 and Table 3. In general, each target sample in the large-incidence-angle images is distributed in a higher-value area, but the small-incidence-angle images exhibit a larger sample distribution range. The VV–HH and $\pi/4$ modes yield optimal or suboptimal results and show good information consistency with the FP. The DCP and CTLR results are almost identical, and their difference measurement results with the FP entropy are also relatively consistent. At different incidence angles in the same oil spill scenario (Scenarios 2 and 3), the VV–HH and $\pi/4$ modes perform well. In the large-incidence-angle scenario, the VV–HH mode is better, but the $\pi/4$ mode is better in the smaller incidence angle. This performance is also verified in Scenario 1 (large incidence angle) and Scenario 4 (small incidence angle). A regular pattern in data distribution is evident: for large-incidence-angle data, the VV–HH and $\pi/4$ entropies are overall lower than the FP, whereas small-incidence-angle data exhibit the opposite tendency. Therefore, these results suggest that across scenarios, the $\pi/4$ mode has the best information consistency with the FP in small-incidence-angle images, whereas the VV–HH mode exhibits the best performance in large-incidence-angle cases. These findings can serve as a reference and guidance for selecting advantageous modes at different incidence angles conditions in the future.

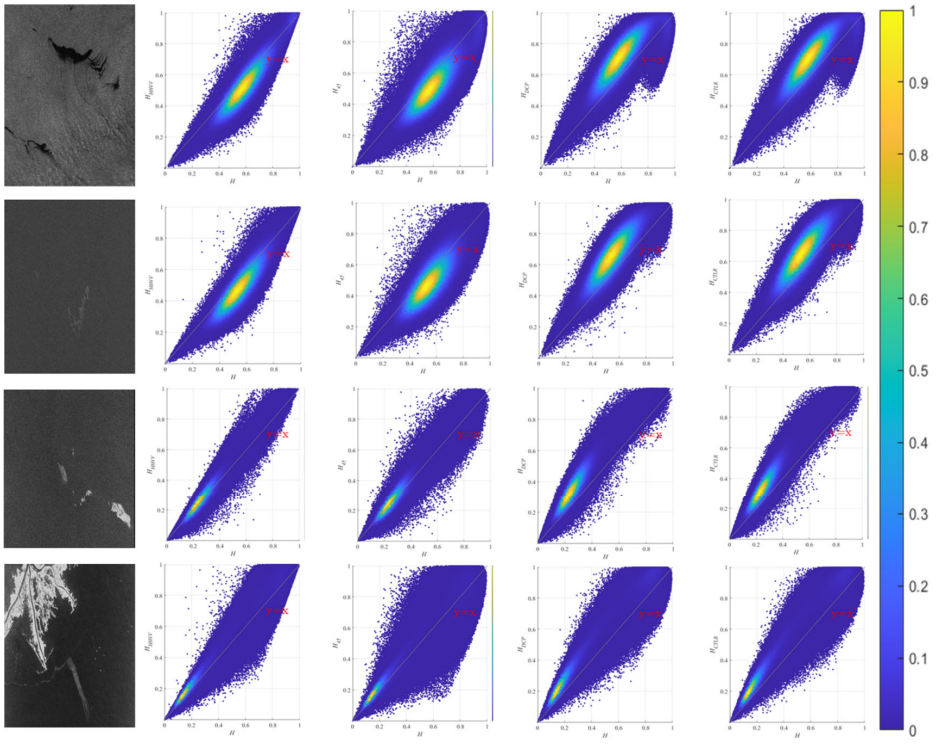
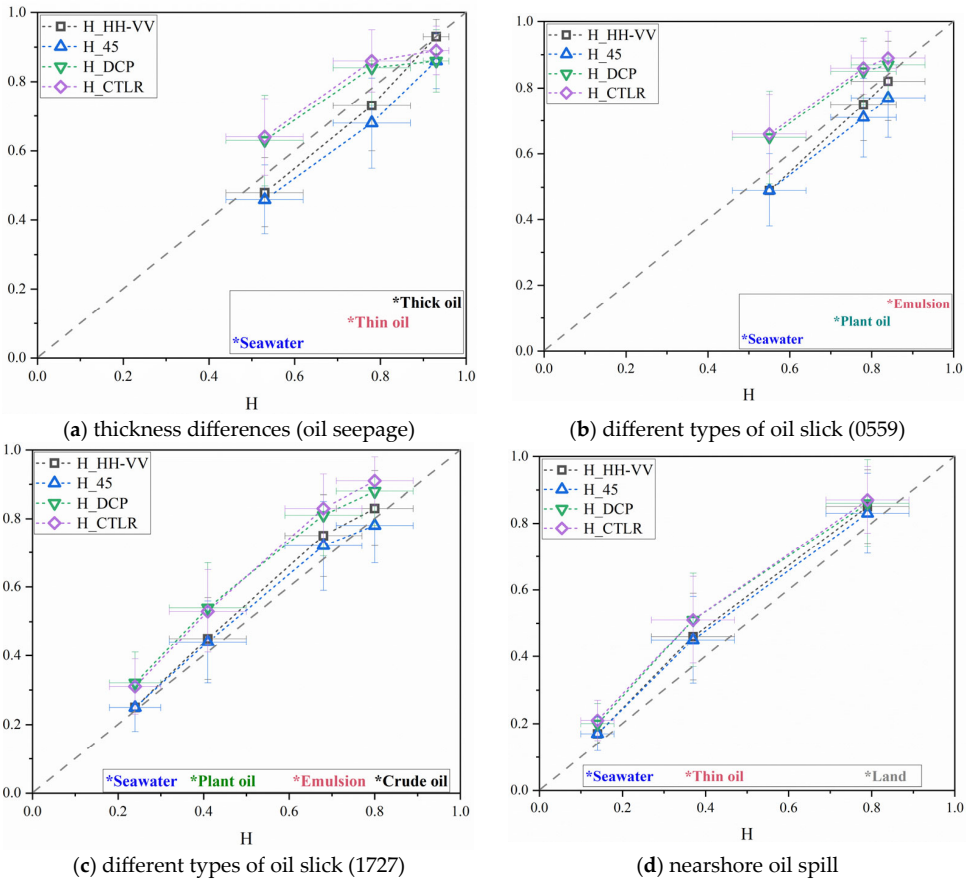


**Figure 5.** Comparison of entropy results between the DP/CP and FP modes. From left to right, the columns are the original visualization, $H_{VV-HH}$ vs. $H$, $H_{\pi/4}$ vs. $H$, $H_{DCP}$ vs. $H$, and $H_{CTLR}$ vs. $H$.




(**a**) thickness differences (oil seepage)

(**b**) different types of oil slick (0559)

(**c**) different types of oil slick (1727)

(**d**) nearshore oil spill

**Figure 6.** Data distribution relationship between FP and DP/CP entropies of sample areas.

**Table 3.** Statistical comparison between FP and DP/CP entropies across oil spill scenarios.

| Class Label | | Index | Mean/MAE/RMSE | | | | |
|---|---|---|---|---|---|---|---|
| | | | $FP_{(Mean)}$ | $H_{VV\text{-}HH}$ | $H_{\pi/4}$ | $H_{DCP}$ | $H_{CTLR}$ |
| Scene 1 | Radarsat-2: Thickness Differences | Thick oil | 0.9266 | **0.931** | 0.857 | 0.862 | 0.887 |
| | | | | **0.0314** | 0.0826 | 0.0663 | 0.0634 |
| | | | | **0.0407** | 0.1023 | 0.0839 | 0.0807 |
| | | Thin oil | 0.7753 | **0.731** | 0.679 | 0.841 | 0.855 |
| | | | | **0.0600** | 0.1066 | 0.0962 | 0.0886 |
| | | | | **0.0746** | 0.1272 | 0.1102 | 0.1035 |
| | | Sea | 0.5304 | **0.475** | 0.464 | 0.633 | 0.642 |
| | | | | **0.0611** | 0.0756 | 0.1192 | 0.1141 |
| | | | | **0.0740** | 0.0915 | 0.1314 | 0.1265 |
| Scene 2 | Radarsat-2: Oil Type Differences | Emulsion | 0.8351 | **0.822** | 0.775 | 0.874 | 0.887 |
| | | | | **0.0450** | 0.0833 | 0.0756 | 0.0742 |
| | | | | **0.0572** | 0.1031 | 0.0951 | 0.0893 |
| | | Plant oil | 0.7800 | **0.753** | 0.711 | 0.854 | 0.8607 |
| | | | | **0.0514** | 0.0877 | 0.0945 | 0.0876 |
| | | | | **0.0632** | 0.1057 | 0.1147 | 0.1011 |
| | | Sea | 0.5550 | **0.493** | 0.492 | 0.6509 | 0.661 |
| | | | | **0.0682** | 0.0766 | 0.1229 | 0.1096 |
| | | | | **0.0816** | 0.0938 | 0.1259 | 0.1237 |
| Scene 3 | Radarsat-2: Oil Type Differences | Crude oil | 0.7971 | 0.828 | **0.78** | 0.878 | 0.911 |
| | | | | **0.0496** | 0.0605 | 0.1021 | 0.1145 |
| | | | | **0.0606** | 0.0746 | 0.1132 | 0.1251 |
| | | Emulsion | 0.6843 | 0.745 | **0.716** | 0.809 | 0.826 |
| | | | | 0.0683 | **0.0622** | 0.1452 | 0.1421 |
| | | | | 0.0798 | **0.0770** | 0.1529 | 0.1506 |
| | | Plant oil | 0.4135 | 0.450 | **0.440** | 0.5431 | 0.533 |
| | | | | 0.0463 | **0.0444** | 0.1401 | 0.1201 |
| | | | | 0.0568 | **0.0559** | 0.1495 | 0.1309 |
| | | Sea | 0.2352 | 0.251 | **0.249** | 0.319 | 0.314 |
| | | | | **0.0236** | 0.0240 | 0.0906 | 0.0804 |
| | | | | **0.03** | 0.0307 | 0.0996 | 0.0904 |
| Scene 4 | Radarsat-2: Nearshore Oil Spill | Thick oil | 0.3700 | 0.460 | **0.453** | 0.508 | 0.506 |
| | | | | 0.0907 | **0.0839** | 0.1437 | 0.1366 |
| | | | | 0.0982 | **0.0926** | 0.1527 | 0.1458 |
| | | Sea | 0.1444 | 0.173 | **0.172** | 0.201 | 0.206 |
| | | | | 0.0295 | **0.0286** | 0.0608 | 0.0617 |
| | | | | 0.0337 | **0.0331** | 0.0672 | 0.0680 |
| | | Land | 0.7922 | 0.846 | **0.826** | 0.861 | 0.869 |
| | | | | **0.0686** | 0.0814 | 0.0941 | 0.0875 |
| | | | | **0.0827** | 0.0995 | 0.1097 | 0.1029 |

$$Mean = \frac{\sum_{i=1}^{n} x_i}{n}$$
$x_i$: each data value
$n$: sample number

$$MAE = \frac{\sum_{i=1}^{n} |x_i - \hat{x}_i|}{n}$$
$x_i$: actual values
$\hat{x}_i$: predicted values
$n$: sample number

$$RMSE = \sqrt{\frac{1}{n}\sum_{i=1}^{n}(x_i - \hat{x}_i)^2}$$
$x_i$: actual values
$\hat{x}_i$: predicted values
$n$: sample number

Furthermore, we compare the mean, mean absolute error (MAE), and root mean square error (RMSE) between the different DP/CP and FP entropy. We comprehensively compare entropy between the FP mode and the DP and CP modes. The results are shown in Table 3, where the bold-face figures are the best results. These comprehensive data present a consistent conclusion: the results for the three assessment indicators are generally highly consistent. In the large-incidence-angle scenario, the mean value of the VV–HH mode has the highest consistency with FP, and the lowest MAE and RMSE results. In the low-incidence-angle scenario, the $\pi/4$ mode has the highest consistency with the FP. Despite the presence of some exceptional results in the two scenarios with low incidence angles for crude oil and land, the VV–HH mode has the lowest MAE and RMSE and the $\pi/4$ mode still slightly outperforms the VV–HH mode, consistent with the results presented

in Figure 6. Additionally, the DCP and CTLR results show good consistency, with CTLR being slightly better. Considering that the different oil spill scenarios vary in aspects such as oil spill causes, sea conditions, ocean area properties, and observation times, minor differences in the subsequent quantitative analysis are within a reasonable range.

### 4.3. Oil Spill Identification Capability of Typical Polarimetric Features Under DP/CP and FP Modes

Based on the definition of the MC measure in Way (1), we compute the contrast degree between the DP/CP and FP entropies under different oil spill scenarios. The results are shown in Table 4 and Figure 7. Overall, the results in Table 4 are highly consistent with the aforementioned conclusions in Section 4.2. In the oil spill scenarios with large incidence angles, the VV–HH mode is closest to the FP mode, having the smallest MC difference. Thus, among the four modes, the VV–HH mode has the smallest entropy contrast with the FP mode. Additionally, the DCP and CTLR modes show good results. In the oil spill scenarios with small incidence angles, the MC result of the $\pi/4$ mode is the lowest, further supporting the regularity results of the previous comparison.

**Table 4.** MC results of different entropies in sample areas across oil spill scenarios.

| Data Scenario/Class Label | Measurement Index | | MC | | | |
|---|---|---|---|---|---|---|
| | | | $H_{VV\text{-}HH}$ | $H_{\pi/4}$ | $H_{DCP}$ | $H_{CTLR}$ |
| Scene 1 | Radarsat-2: Thickness Differences | Thick oil | **0.004** | 0.0461 | 0.0341 | 0.0352 |
| | | Thin oil | **0.0333** | 0.0708 | 0.0544 | 0.0497 |
| | | Sea | **0.0583** | 0.0707 | 0.0994 | 0.0951 |
| Scene 2 | Radarsat-2: Oil Type Differences | Emulsion | **0.0106** | 0.0409 | 0.0341 | 0.0306 |
| | | Plant oil | **0.0205** | 0.0499 | 0.0557 | 0.0492 |
| | | Sea | **0.0637** | 0.064 | 0.0912 | 0.0868 |
| Scene 3 | Radarsat-2: Oil Type Differences | Crude oil | 0.0182 | **0.0125** | 0.0598 | 0.0681 |
| | | Emulsion | 0.0404 | **0.0195** | 0.0964 | 0.0949 |
| | | Plant oil | 0.0379 | **0.0271** | 0.1437 | 0.1259 |
| | | Sea | 0.0282 | **0.0251** | 0.1585 | 0.1412 |
| Scene 4 | Radarsat-2: Nearshore Oil Spill | Thick oil | 0.1071 | **0.0998** | 0.1625 | 0.1552 |
| | | Sea | 0.0882 | **0.0855** | 0.1703 | 0.1726 |
| | | Land | 0.0322 | **0.0196** | 0.0516 | 0.0464 |

Oil spill identification and extraction are based on discrimination between targets. The OR between target samples can quantify the confusion degree and evaluate the target classification ability in the corresponding feature space. We compute the OR between target samples with different polarimetric modes across scenarios. All samples in the same scenario are randomly extracted in the same quantity for unified, effective quantitative comparison and analysis. The results are shown in Table 5. In the four oil spill scenarios, regardless of incidence angle, the best results are almost all in the FP mode. Among the DP and CP modes, the VV–HH mode in the large-incidence-angle oil spill scenario has the lowest OR between targets and is closest to the FP result, with a difference range of 0.77–6.48%. At a low incidence angle, the CTLR mode has the best OR between targets and exhibits a difference range of 0–5.83% compared with the FP result. In addition, the DCP and CTLR modes show similar target results.

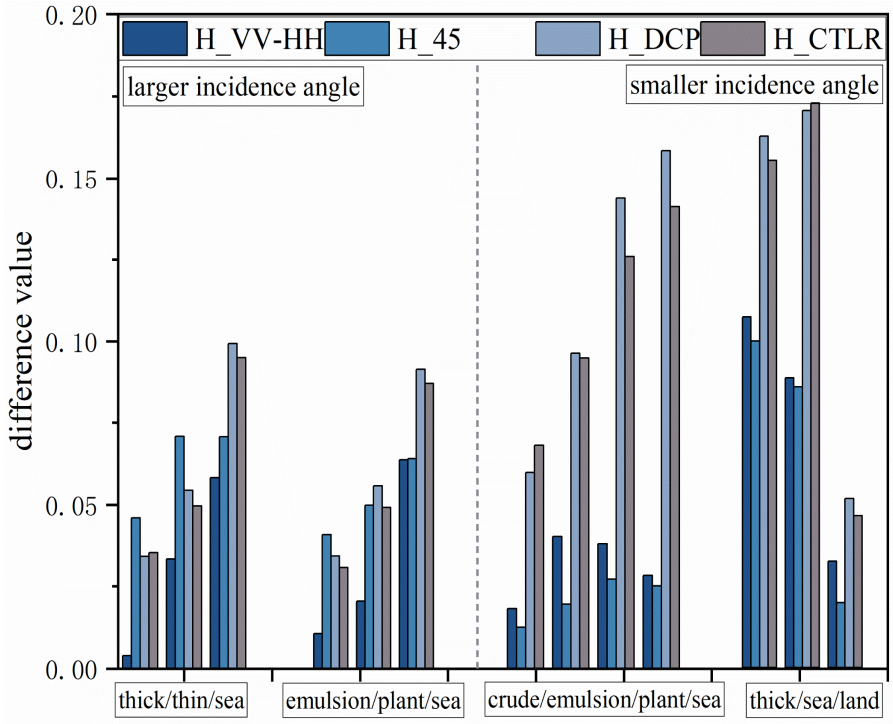



**Figure 7.** Visualization of MC ranking results for the DP/CP and FP modes.

**Table 5.** OR values of feature parameters under the FP, DP, and CP modes across oil spill scenarios.

| Class Label | Index | Overlap | | | | |
|---|---|---|---|---|---|---|
| | | $H_FP$ | $H_{VV\text{-}HH}$ | $H_{\pi/4}$ | $H_{DCP}$ | $H_{CTLR}$ |
| Scene 1 | Thick-Sea | 0.38% | **1.15%** | 3.88% | 19.72% | 18.22% |
| | Thin-Sea | 19.68% | **25.76%** | 34.18% | 29.53% | 28.34% |
| | Thick-Thin | 22.57% | **26.18%** | 35.41% | 88.00% | 82.62% |
| Scene 2 | Emulsion-Sea | 6.19% | **8.63%** | 15.35% | 21.24% | 16.24% |
| | Plant-Sea | 26.71% | **33.19%** | 39.20% | 42.18% | 34.15% |
| | Emulsion-Plant | 45.75% | **50.45%** | 58.95% | 69.13% | 64.13% |
| Scene 3 | Crude-Sea | 0.94% | 1.66% | 2.81% | **0.94%** | 1.46% |
| | Emulsion-Sea | 3.12% | 5.52% | 4.99% | 5.72% | **3.33%** |
| | Plant-Sea | 24.97% | 33.19% | 34.76% | 35.07% | **28.82%** |
| | Crude-Plant | 5.52% | 16.34% | 20.29% | 16.02% | **7.28%** |
| | Emulsion-Plant | 28.72% | 35.17% | 39.23% | 38.71% | **32.26%** |
| | Crude-Emulsion | 46.62% | 56.3% | 63.27% | 64.1% | **52.45%** |
| Scene 4 | Oil-Sea | 5.31% | 6.56% | 6.56% | 6.87% | **5.83%** |
| | Oil-Land | 0.21% | **4.58%** | 4.79% | 10.41% | 11.13% |

In the studied multisource oil spill scenario, different results are obtained for $H_A$. Tables 5 and 6 present the image data obtained at two imaging times at different incidence angles in the same oil spill scenario. According to the visualization results and target comparisons in Figure 8 and Tables 5–7, among the four $H_A$ combination results under each polarimetric mode, $H(1-A)$ and $A(1-H)$ perform well in different oil spill scenarios. This is attributed to the enhancement effect of the mathematical combination in the parameter calculation on target distinction. In the various oil spill scenarios, the best separation results between different targets are not always based on the FP mode; the DP and CP modes also show advantages and potential. As for the contrast between different types of oil slick

targets at a large incidence angle, the FP mode performs best in the $HA$ and $(1-H)(1-A)$ combinations. As for the $H(1-A)$ and $A(1-H)$ combinations, the VV–HH mode performs better, followed by the DCP and CTLR modes, which show similar results. Regarding the contrast between different types of oil slick targets at a small incidence angle, the FP mode still presents the highest contrast between various targets in the $HA$ and $(1-H)(1-A)$ combinations. In addition, the CTLR (DCP) mode outperforms the VV–HH mode. The VV–HH mode outperforms the FP mode, whereas the DCP and CTLR modes have basically the same results, showing certain potential in oil spill identification.

**Table 6.** MC of $H_A$ combination under different modes at large incidence angles in Norway.

| Inter-Class \ Feature | | ***FP*** | **VV-HH** | **π/4** | **DCP** | **CTLR** |
|---|---|---|---|---|---|---|
| Emulsion—Sea | $HA$ | **0.1833** | 0.0263 | 0.0126 | 0.1487 | 0.1439 |
| | $H(1-A)$ | 0.2088 | **0.5968** | 0.5373 | 0.3953 | 0.3996 |
| | $A(1-H)$ | 0.4575 | 0.6058 | 0.501 | **0.6487** | 0.6316 |
| | $(1-H)(1-A)$ | **0.4601** | 0.1379 | 0.0682 | 0.2886 | 0.2808 |
| Inter-Class \ Feature | | FP | VV-HH | π/4 | DCP | CTLR |
| Plant oil—Sea | $HA$ | **0.1603** | 0.0294 | 0.0426 | 0.1101 | 0.0965 |
| | $H(1-A)$ | 0.1719 | **0.5028** | 0.4417 | 0.3604 | 0.3544 |
| | $A(1-H)$ | 0.3484 | 0.4584 | 0.3709 | **0.5762** | 0.5454 |
| | $(1-H)(1-A)$ | **0.3343** | 0.0382 | 0.0058 | 0.2272 | 0.2042 |
| Inter-Class \ Feature | | FP | VV-HH | π/4 | DCP | CTLR |
| Emulsion—Plant | $HA$ | 0.0237 | **0.0557** | 0.03 | 0.0393 | 0.048 |
| | $H(1-A)$ | 0.0383 | **0.1344** | 0.1254 | 0.0408 | 0.0526 |
| | $A(1-H)$ | 0.1298 | **0.204** | 0.1599 | 0.1157 | 0.1316 |
| | $(1-H)(1-A)$ | **0.1486** | 0.1002 | 0.0624 | 0.0657 | 0.0812 |

**Table 7.** MC of $H_A$ combination under different modes at small incidence angles in Norway.

| **Inter-Class** \ **Feature** | | **FP** | **VV-HH** | **π/4** | **DCP** | **CTLR** |
|---|---|---|---|---|---|---|
| Crude/Sea | $HA$ | **0.4351** | 0.2262 | 0.2691 | 0.0249 | 0.018 |
| | $H(1-A)$ | 0.6111 | **0.9032** | 0.8864 | 0.865 | 0.8791 |
| | $A(1-H)$ | 0.6552 | 0.7646 | 0.6892 | 0.8553 | **0.8849** |
| | $(1-H)(1-A)$ | **0.5218** | 0.1239 | 0.2017 | 0.1609 | 0.1916 |
| Inter-Class \ Feature | | FP | VV-HH | π/4 | DCP | CTLR |
| Emulsion/Sea | $HA$ | **0.4784** | 0.2708 | 0.2812 | 0.1169 | 0.1397 |
| | $H(1-A)$ | 0.497 | **0.8722** | 0.8614 | 0.8315 | 0.8397 |
| | $A(1-H)$ | 0.4255 | 0.6265 | 0.5811 | 0.7329 | **0.7359** |
| | $(1-H)(1-A)$ | **0.4073** | 0.2192 | 0.2412 | 0.0032 | 0.03 |
| Inter-Class \ Feature | | FP | VV-HH | π/4 | DCP | CTLR |
| Plant/Sea | $HA$ | **0.2854** | 0.2167 | 0.2134 | 0.1643 | 0.1711 |
| | $H(1-A)$ | 0.2653 | **0.6053** | 0.5953 | 0.5738 | 0.5661 |
| | $A(1-H)$ | 0.1199 | 0.2068 | 0.1973 | **0.2745** | 0.2568 |
| | $(1-H)(1-A)$ | 0.1425 | **0.2273** | 0.2247 | 0.1546 | 0.166 |

**Table 7.** *Cont.*

| Inter-Class \ Feature | | FP | VV-HH | $\pi/4$ | DCP | CTLR |
|---|---|---|---|---|---|---|
| Crude/Plant | $HA$ | **0.1709** | 0.0099 | 0.0591 | 0.1399 | 0.1536 |
| | $H(1-A)$ | 0.4128 | **0.6571** | 0.6163 | 0.5783 | 0.6231 |
| | $A(1-H)$ | 0.5809 | 0.6626 | 0.5693 | 0.759 | **0.8128** |
| | $(1-H)(1-A)$ | **0.4097** | 0.1064 | 0.0241 | 0.3079 | 0.3465 |
| Inter-Class \ Feature | | FP | VV-HH | $\pi/4$ | DCP | CTLR |
| Emulsion/Plant | $HA$ | **0.2235** | 0.0574 | 0.0722 | 0.0483 | 0.0322 |
| | $H(1-A)$ | 0.2669 | **0.5654** | 0.5461 | 0.493 | 0.5216 |
| | $A(1-H)$ | 0.322 | 0.4821 | 0.4335 | 0.5739 | **0.5908** |
| | $(1-H)(1-A)$ | **0.2811** | 0.0086 | 0.0174 | 0.1515 | 0.1366 |
| Inter-Class \ Feature | | FP | VV-HH | $\pi/4$ | DCP | CTLR |
| Crude/Emulsion | $HA$ | 0.0547 | 0.0475 | 0.0131 | 0.0922 | **0.122** |
| | $H(1-A)$ | **0.1639** | 0.1459 | 0.1058 | 0.1193 | 0.1503 |
| | $A(1-H)$ | 0.3185 | 0.2652 | 0.1802 | 0.3281 | **0.4272** |
| | $(1-H)(1-A)$ | 0.1454 | 0.0979 | 0.0415 | 0.164 | **0.2203** |

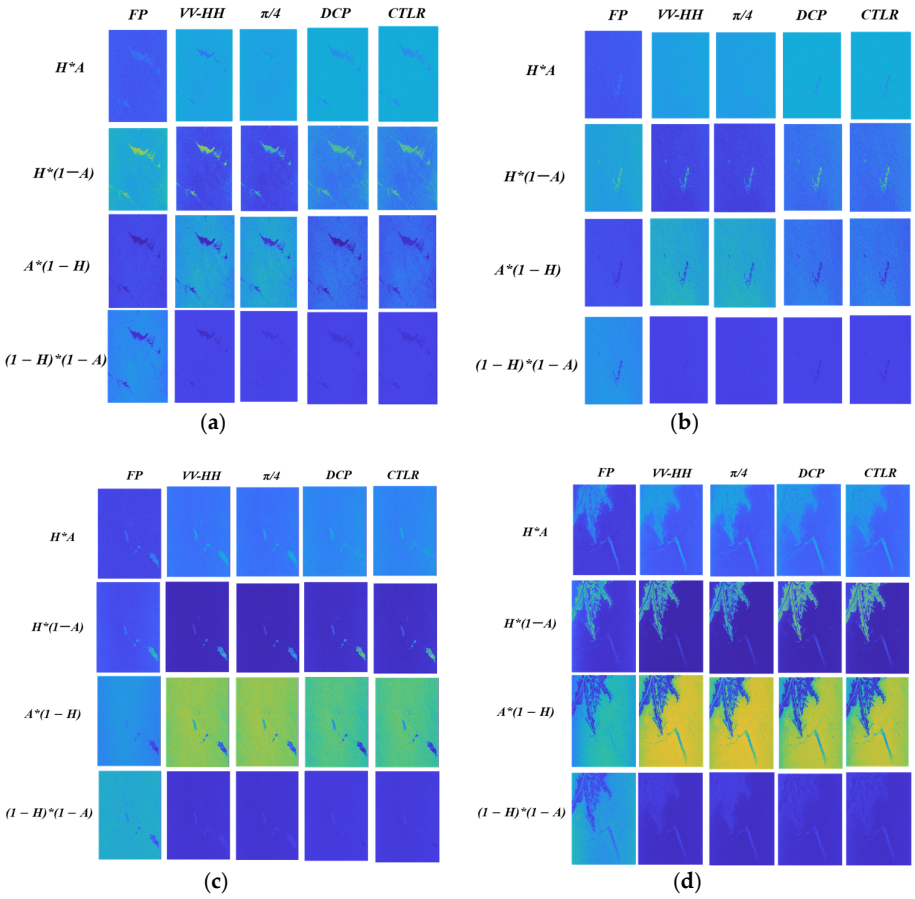



**Figure 8.** Visualization of H_A combination feature across oil spill scenarios under different DP/CP and FP modes. (**a**) thickness differences (oil seepage), (**b**) different types of oil slick (large incidence angle; 0559) (**c**), different types of oil slick (small incidence angle; 1729), and (**d**) nearshore oil spill.

Portions of the polarimetric information in the FP data are also shared the DP and CP data, retaining the same physical significance in the self-similarity results. Therefore, the DP/CP and FP modes exhibit unified similarity in specific target areas. In other words, the self-similarity of single scattering mechanism targets (e.g., clean sea surface) is high, whereas targets with high scattering mechanism complexity (e.g., land and oil slicks) have low self-similarity. However, the polarimetric modes perform differently across scenarios. According to the visualization results, the DCP and CTLR modes are consistent with the self-similarity results of the FP system across scenarios. In addition, for the images with large incidence angles, such as in the natural oil seepage scenario and the Norwegian spill experiment data, seawater has lower self-similarity values compared to smaller-incidence-angle scenarios, indicating complex target scattering mechanisms in these two scenarios. Among them, the phenomena of the FP, DCP, and CTLR modes are evident. This may be because the data in the large-incidence-angle scenarios are more affected by background noise and multiple scattering mechanisms, resulting in high randomness and complexity.

The self-similarity parameters of targets under different polarization modes (FP, DP, and CP modes) across scenarios are compared in the Figures 9 and 10. The self-similarity results of the FP mode substantially vary between targets with different scattering mechanisms, and its overall values are low compared with those of the other polarization modes. The DCP and CTLR modes have the closest results to the FP mode, especially for plant oil slick and seawater targets. However, their gradient change between various targets is smoother relative to that under the FP mode.

We compare the MC results between targets for the self-similarity parameters of the FP, DP, and CP modes across the four oil spill scenario datasets in Table 8. Based on these results, we evaluate oil spill recognition capabilities across polarization modes. The FP can achieve the highest contrast results in all comparison tasks, especially for mineral oil targets. For the DP and CP modes, the corresponding targets exhibit similar scattering characteristics. In the oil spill scenarios with large incidence angles, the VV–HH mode has the best MC result. As for the low-incidence-angle oil spill scenarios, the DCP and CTLR modes exhibit almost the same results and perform the best.

**Table 8.** Differences between self-similarity parameters of oil spill targets under DP, CP, and FP modes.

| Class Label | Index | MC-$rrr_s$ | | | | |
|---|---|---|---|---|---|---|
| | | **FP** | **VV-HH** | **π/4** | **DCP** | **CTLR** |
| Scene 1 | Thick—Sea | 0.2834 | **0.1973** | 0.1599 | 0.1098 | 0.115 |
| | Thin—Sea | 0.1565 | 0.0961 | 0.0776 | **0.0994** | 0.0973 |
| | Thick—Thin | 0.1327 | **0.1031** | 0.0833 | 0.0105 | 0.0179 |
| Scene 2 | Emulsion—Sea | 0.191 | **0.1333** | 0.1106 | 0.1078 | 0.1073 |
| | Plant—Sea | 0.147 | **0.1003** | 0.0819 | 0.0962 | 0.0927 |
| | Emulsion—Plant | 0.0453 | **0.0304** | 0.029 | 0.0117 | 0.0148 |
| Scene 3 | Crude—Sea | 0.2935 | 0.2002 | 0.1773 | 0.2183 | **0.2287** |
| | Emulsion—Sea | 0.2196 | 0.1614 | 0.1493 | 0.1832 | **0.1843** |
| | Plant—Sea | 0.0712 | 0.0526 | 0.0502 | **0.0684** | 0.0641 |
| | Crude—Plant | 0.2271 | 0.1492 | 0.1283 | 0.1521 | **0.167** |
| | Emulsion—Plant | 0.1508 | 0.1097 | 0.0999 | 0.1162 | **0.1217** |
| | Crude—Emulsion | 0.079 | 0.0402 | 0.0287 | 0.0366 | **0.0463** |
| Scene 4 | Oil-Sea | 0.0848 | 0.0723 | 0.0703 | **0.0828** | 0.0803 |
| | Land—Sea | 0.3189 | 0.2247 | 0.2152 | **0.2347** | 0.2302 |
| | Oil—Land | 0.2406 | 0.153 | 0.1472 | **0.1549** | 0.1527 |

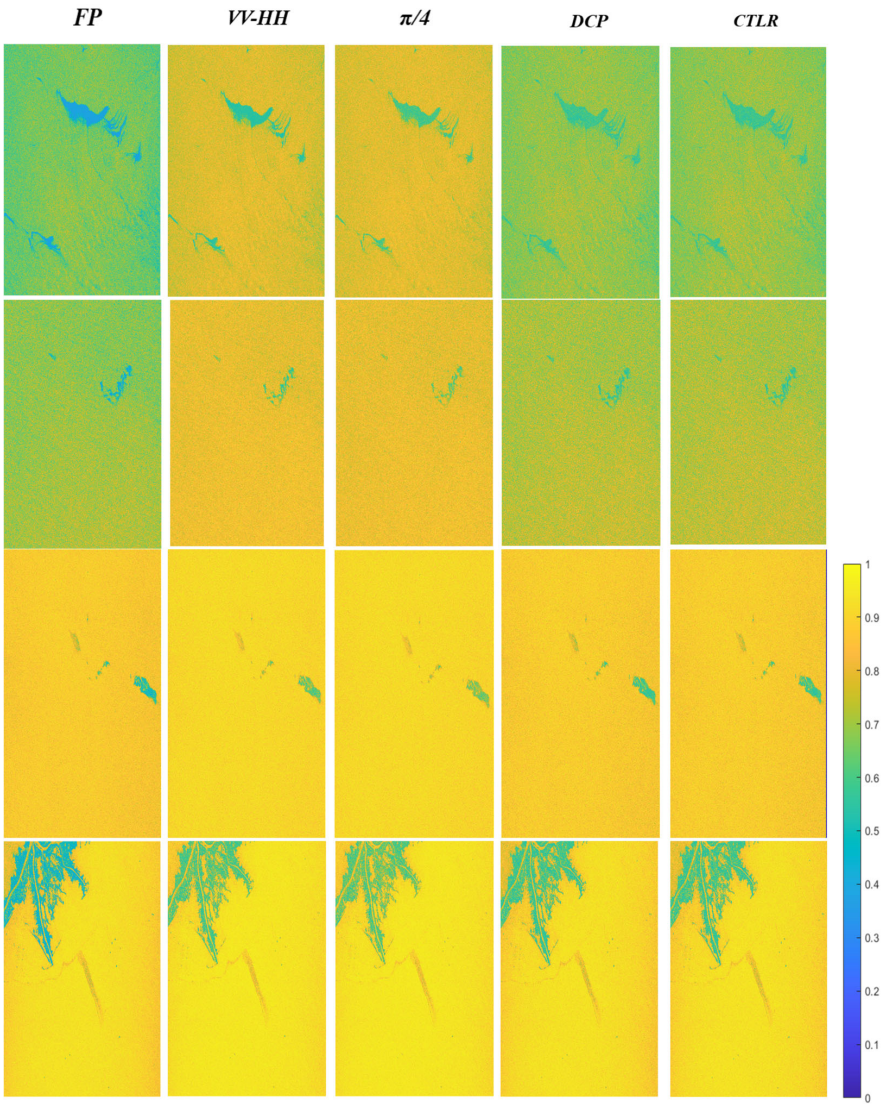



**Figure 9.** Visualization of self-similarity under different DP/CP and FP modes across oil spill scenarios. The rows denote the oil spill scenarios: natural oil seepage, different types of oil slick (large incidence angle), different types of oil slick (small incidence angle), and nearshore oil spill. From left to right, the columns are the FP, VV–HH, $\pi/4$, DCP. and CTLR.

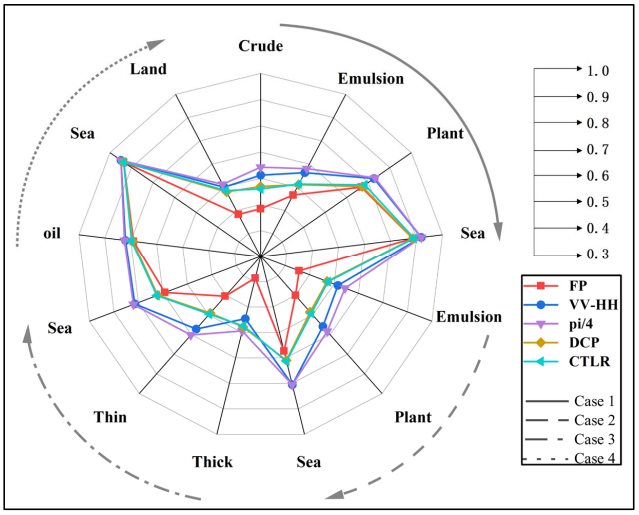



**Figure 10.** Self-similarity between the DP/CP and FP modes across oil spill scenarios.

## 5. Discussion

### 5.1. Relative Distributions of Instrument Noise and NRCS Across Oil Spill Scenarios

The sea surface covered by oil slick will exhibit a low NRCS value due to the reduced backscattering signal strength, which is closer to or even lower than the noise floor (NESZ baseline), whereas the surrounding seawater area shows a high NRCS value. The four oil spill scenarios are qualitatively divided into large incidence angles (Scenarios 1 and 2) and small incidence angles (Scenarios 3 and 4). Scenarios 2 and 3 are the same oil spill experiment in the same sea area at two incidence angles within a 24 h interval. Overall, across the four scenarios, the co-polarization channels generally show higher signal levels than the cross-polarization channel. Between the co-polarization channels, HH undergoes faster attenuation of the echo signal, so its signal strength is closer to the noise baseline. The high-incidence-angle images are more contaminated by noise, with the co-polarization channels exhibiting considerable differences. The low-incidence-angle images are less affected by noise, and their signals remain above the NESZ baseline overall. Regarding the distribution of target signals in the cross-polarization channel, regardless of incidence angle, a considerable proportion of samples fall below the NESZ baseline, with severe signal confusion except in the case of land targets. These phenomena lead to notable differences in the influence degree of image noise on the target samples under varying observation conditions, potentially affecting the subsequent expression of polarimetric scattering characteristics and exhibiting a certain regular influence on the quantification of polarimetric features. This can also explain why the scattering randomness of the seawater target samples in Scenarios 1 and 2 is generally higher than that in Scenarios 3 and 4, even without considering the differences in causes of oil slick formation in various sea areas. Although Scenarios 2 and 3 were obtained from the same sea area and the same oil spill experiment at similar times, the background seawater in the two scenarios shows a considerable difference in signal levels. The possible effect of polarimetric features is discussed in the next section.

### 5.2. Oil Spill Identification for Typical Polarimetric Features Under DP/CP Mode

The comprehensive analysis of oil spill identification capabilities under various DP/CP modes mainly focuses on two aspects. First, it explores the degree of information consistency between the DP/CP and FP modes at different incidence angles. Second, it evaluates the ability of DP/CP modes to represent differences in oil spill information across multiple scenarios and incidence angles conditions.

Polarimetric scattering entropy, self-similarity, and *H_A* combination features are commonly used in marine oil spills, and they are important indicators for quantifying the scattering characteristics of targets (e.g., randomness). They were adopted and verified for effectiveness using the FP mode of the utilized dataset. Then, the comparison and analysis are extended to the FP, DP, and CP modes. In this study, mineral oil was released and subjected to dispersion and mechanical recovery under certain marine experimental conditions [4]. In particular, emulsion underwent certain degrees of weathering and diffusion before satellite passage. This involved a series of physical and chemical processes affecting the characterization of oil slick complexity and randomness. Therefore, the complexity of mineral oil is higher than that of plant oil, both in backscattering intensity and typical polarimetric features. SAR is capable of imaging any scattering process that influences Bragg surface roughness. The oil area damps the ocean capillary and gravity waves (i.e., the Bragg waves in certain radar wavelengths),and presents with complex characteristics due to the presence of multiple scattering mechanisms, such as Bragg and non-Bragg scattering [36]. The above situation can be analyzed in terms of two aspects: First, in combination with Section 5.1, the target signals in the high-incidence-angle

scenarios are affected by instrument noise because they are close to the NESZ baseline, presenting more complex random scattering characteristics. Second, according to a previous study [8], "When incidence angles are near 45°, especially at the grazing angle, Multipath Dihedral-Type Features are potentially important ocean surface scatterers." This increases the randomness of the scattering mechanism on the sea surface. This further explains that the polarimetric entropy values of the two high-incidence-angle scenarios are overall higher than those of the low-incidence-angle scenarios. Other typical polarimetric features also exhibit similar regular differences at varying incidence angles. These fluctuations are due to the differences in polarimetric scattering characteristics between targets. In the various oil spill scenarios, at high incidence angles, VV–HH exhibits the best performance, regardless of information consistency with FP or oil–water information differences. At low incidence angles, the CP mode performs best in terms of consistency and oil–water information differentiation, especially the CTLR mode. In addition, the comparison and identification of oil slick information under different polarization modes rely on a comprehensive analysis and interpretation of the data information. By combining machine learning methods to construct datasets across multiple scenarios and detection conditions, it is beneficial to select the optimal mode.

## 6. Conclusions

This study investigates different DP and CP modes based on FP data in multisource oil spill scenarios. Their information consistency with FP is determined, and the oil spill identification capabilities of typical polarimetric features are compared. This comparative analysis not only focuses on the information consistency and characteristic differences of multiple modes in different sea areas and for various oil spill causes; it also considers the advantages of different modes at various incidence angles.

This study shows that in oil spill scenarios with small incidence angles, various targets (oil spill targets and background information) are less affected by the NESZ baseline, the signal difference between oil and seawater is large, and the gradient change between co-polarization channels VV and HH is shallow. In oil spill scenarios with large incidence angles, the results are the opposite. Regarding typical oil spill features, at large incidence angles, the VV–HH mode performs better in terms of information consistency with the FP mode and in terms of separation and confusion degree between the oil spill target and the surrounding background information. In the case of small incidence angles, the CP mode presents a more comprehensive optimal result, among which the polarimetric entropy of the $\pi/4$ mode shows stronger information consistency with the FP mode. The CTLR mode shows the best performance among various typical polarimetric feature sets in terms of oil–water differentiation. Additionally, the DCP and CTLR modes have similar results in quantitative comparisons of oil–water contrast and sample confusion degree. Finally, the $H_A$ feature combination $H(1-A)$ and $A\,(1-H)$ demonstrates superiority in inter-class contrast discrimination under most DP/CP conditions. Moreover, in terms of identifying differences between multiple target scenarios, the FP system does not always achieve the optimal result. The DP and CP modes demonstrate excellent potential from different perspectives, regardless of oil slick types and incidence angles.

This study compares and analyzes the information consistency and oil spill target extraction capabilities of various polarimetric modes in different oil spill scenarios, further demonstrating the potential of the CP mode in oil spill detection. It also provides guidance and a reference for the selection of advantageous polarimetric modes for future oil spill monitoring applications at different incidence angles. It is worth noting that this study was conducted through qualitative and quantitative analysis based on a limited dataset of oil spill scenarios and conditions. Other tests may show the results differences due

to variations in sensors, causes of oil spills, observation conditions, etc. Future research will focus on enriching our results under more extensive sensor, oil spill scenario, and incidence angle conditions. We will also conduct simulations and analyses to compare the sensor-specific attributes such as the noise floor of different DP/CP modes with the FP mode, in addition, comparative studies on different types of feature parameters derived from multiple polarimetric modes in various oil spill scenarios by combining machine learning algorithms.

**Author Contributions:** Conceptualization, G.L. (Guannan Li) and G.L. (Gaohuan Lv); writing—original draft preparation, G.L. (Guannan Li).; writing—review and editing, G.L. (Gaohuan Lv) and B.L.; visualization and supervision, X.W. and F.Z.; funding acquisition, F.Z. All authors have read and agreed to the published version of the manuscript.

**Funding:** This research is supported by the National Natural Science Foundation of China (No. 52505110), the Natural Science Foundation of Shandong Province (Grant No. ZR2024QD174, ZR2025QC528, ZR2025QC1130), and the Shandong Province Youth Innovation Team for Higher Education Institutions (2024KJG061). Technological Small and Medium-sized Enterprises Innovation Ability Enhancement Project of Shandong Province (Grant No. 2024TSGC0757) also supported this project.

**Data Availability Statement:** Data available upon reasonable request from the authors.

**Acknowledgments:** We appreciate the valuable comments provided by the anonymous reviewers and editors, which helped improve the manuscript. We thank Shiyong Wen of the National Marine Environmental Monitoring Center for the data processing and Rui Guo of Northwestern Polytechnical University for the data-processing.

**Conflicts of Interest:** The authors declare no conflicts of interest.

## Abbreviations

The following abbreviations are used in this manuscript:

| | |
|---|---|
| CP | Compact Polarimetric |
| DP | Dual Polarization |
| FP | Full Polarization |
| MAE | Mean Absolute Error |
| MC | Michelson Contrast |
| NESZ | Noise-Equivalent Sigma Zero |
| NRCS | Normalized Radar Cross Section |
| OR | Overlap Ratio |
| PolSAR | Polarimetric Synthetic-Aperture Radar |
| RMSE | Root Mean Square Error |
| SAR | Synthetic-Aperture Radar |

## References

1. Fingas, M.; Brown, C. A review of oil spill remote sensing. *Sensors* **2017**, *18*, 91. [CrossRef] [PubMed]
2. Fingas, M.; Brown, C.E. Review of oil spill remote sensing: The current state of the art. *Oil Spill Sci. Technol.* **2025**, *2025*, 309–358. [CrossRef]
3. Migliaccio, M.; Nunziata, F.; Buono, A. SAR polarimetry for sea oil slick observation. *Int. J. Remote Sens.* **2015**, *36*, 3243–3273. [CrossRef]
4. Skrunes, S.; Brekke, C.; Eltoft, T. Characterization of marine surface slicks by radarsat-2 multipolarization features. *IEEE Trans. Geosci. Remote Sens.* **2013**, *52*, 5302–5319. [CrossRef]
5. Zhang, B.; Perrie, W.; Li, X.; Pichel, W.G. Mapping sea surface oil slicks using RADARSAT-2 quad-polarization SAR image. *Geophys. Res. Lett.* **2011**, *38*, L10602. [CrossRef]
6. Migliaccio, M.; Gambardella, A.; Nunziata, F.; Shimada, M.; Isoguchi, O. The PALSAR polarimetric mode for sea oil slick observation. *IEEE Trans. Geosci. Remote Sens.* **2009**, *47*, 4032–4041. [CrossRef]

7. Lee, J.-S.; Pottier, E. *Polarimetric Radar Imaging: From Basics to Application*; CRC Press: Boca Raton, FL, USA, 2017.
8. Li, H.; Perrie, W.; He, Y.; Wu, J.; Luo, X. Analysis of the polarimetric SAR scattering properties of oil-covered waters. *IEEE J. Sel. Top. Appl. Earth Obs. Remote Sens.* **2014**, *8*, 3751–3759. [CrossRef]
9. Raney, R.K. Hybrid-polarity SAR architecture. *IEEE Trans. Geosci. Remote Sens.* **2007**, *45*, 3397–3404. [CrossRef]
10. Souyris, J.C.; Imbo, P.; Fjortoft, R.; Mingot, S.; Lee, J.S. Compact polarimetry based on symmetry properties of geophysical media: The /spl Pi//4 Mode. *IEEE Trans. Geosci. Remote Sens.* **2005**, *43*, 634–646. [CrossRef]
11. Stacy, N.; Preiss, M. Compact polarimetric analysis of X-band SAR data. In Proceedings of the EUSAR 2006—6th European Conference on Synthetic Aperture Radar, Dresden, Germany, 16–18 May 2006.
12. Xu, L.; Zhang, H.; Wang, C.; Zhang, B.; Tian, S. Compact polarimetric SAR ship detection with M-δ decomposition using visual attention model. *Remote Sens.* **2016**, *8*, 751. [CrossRef]
13. Ji, K.; Wu, Y. Scattering mechanism extraction by a modified cloude-pottier decomposition for dual polarization SAR. *Remote Sens.* **2015**, *7*, 7447–7470. [CrossRef]
14. Liang, L.; Zhang, Y.; Li, D.; Dong, X. A new entropy estimation method for dual-polarimetric SAR data: Comparative analysis with quad- and other dual-polarization approaches. *IEEE J. Sel. Top. Appl. Earth Obs. Remote Sens.* **2024**, *17*, 847–864. [CrossRef]
15. Rashid, M.; Gierull, C.; Rajan, S. A study of selected constant false alarm rate (CFAR) detectors for vessels with compact and dual polarimetric synthetic aperture radar (SAR). *Can. J. Remote Sens.* **2025**, *51*, 2552891. [CrossRef]
16. Liu, C.-A.; Chen, Z.; Wang, D.; Li, D. Assessment of the X- and C-band polarimetric SAR data for plastic-mulched farmland classification. *Remote Sens.* **2019**, *11*, 660. [CrossRef]
17. Ullmann, T.; Schmitt, A.; Jagdhuber, T. Two component decomposition of dual polarimetric HH/VV SAR data: Case study for the tundra environment of the Mackenzie Delta region, Canada. *Remote Sens.* **2016**, *8*, 1027. [CrossRef]
18. Lv, C.; Xie, Q.; Peng, X.; Dou, Q.; Wang, J.; Lopez-Sanchez, J.M.; Shang, J.; Chen, L.; Fu, H.; Zhu, J. Soil moisture retrieval over agricultural fields with machine learning: A comparison of quad-, compact-, and dual-polarimetric time-series SAR data. *J. Hydrol.* **2024**, *644*, 132093. [CrossRef]
19. Sabry, R. Hybrid products for enhanced and unified full and compact polarimetric SAR data exploitations. *IEEE J. Sel. Top. Appl. Earth Obs. Remote Sens.* **2025**, *18*, 12059–12073. [CrossRef]
20. Shu, S.; Yang, J.; Jing, W.; Yang, C.; Wu, J. Mangrove extraction from compact polarimetric synthetic aperture radar images based on optimal feature combinations. *Forests* **2024**, *15*, 2047. [CrossRef]
21. Zhou, X.; Wang, J.; Shan, B.; He, Y. Soil moisture retrieval over soybean fields during growing season using polarimetric decomposition and time-series RCM data. *Comput. Electron. Agric.* **2025**, *229*, 109935. [CrossRef]
22. Hou, W.; Zhao, F.; Liu, X.; Zhang, H.; Wang, R. A unified framework for comparing the classification performance between quad-, compact-, and dual-polarimetric SARs. *IEEE Trans. Geosci. Remote Sens.* **2021**, *60*, 5204814. [CrossRef]
23. Shirvany, R.; Chabert, M.; Tourneret, J.-Y. Ship and oil-spill detection using the degree of polarization in linear and hybrid/compact dual-pol SAR. *IEEE J. Sel. Top. Appl. Earth Obs. Remote Sens.* **2012**, *5*, 885–892. [CrossRef]
24. Song, G.; Deng, Y.; Zhang, H.; Liu, X.; Chang, S. Improving SAR ship detection accuracy by optimizing polarization modes: A study of generalized compact polarimetry (GCP) performance. *Remote Sens.* **2025**, *17*, 1951. [CrossRef]
25. Buono, A.; Nunziata, F.; Migliaccio, M.; Li, X. Polarimetric analysis of compact-polarimetry SAR architectures for sea oil slick observation. *IEEE Trans. Geosci. Remote Sens.* **2016**, *54*, 5862–5874. [CrossRef]
26. Ebrahimi, M.; Sahebi, M.R. A transfer learning-DCNN based oil spill detection using compact polarimetric SAR data. *Remote Sens. Appl. Soc. Environ.* **2025**, *37*, 101417. [CrossRef]
27. Nunziata, F.; Migliaccio, M.; Li, X. Sea oil slick observation using hybrid-polarity SAR architecture. *IEEE J. Ocean. Eng.* **2014**, *40*, 426–440. [CrossRef]
28. Zhang, B.; Li, X.; Perrie, W.; Garcia-Pineda, O. Compact polarimetric synthetic aperture radar for marine oil platform and slick detection. *IEEE Trans. Geosci. Remote Sens.* **2016**, *55*, 1407–1423. [CrossRef]
29. Li, G.; Li, Y.; Hou, Y.; Wang, X.; Wang, L. Marine oil slick detection using improved polarimetric feature parameters based on polarimetric synthetic aperture radar data. *Remote Sens.* **2021**, *13*, 1607. [CrossRef]
30. Song, D.; Zhen, Z.; Wang, B.; Li, X.; Gao, L.; Wang, N.; Xie, T.; Zhang, T. A novel marine oil spillage identification scheme based on convolution neural network feature extraction from fully polarimetric SAR imagery. *IEEE Access* **2020**, *8*, 59801–59820. [CrossRef]
31. Li, G.; Li, Y.; Liu, B.; Hou, Y.; Fan, J. Analysis of scattering properties of continuous slow-release slicks on the sea surface based on polarimetric synthetic aperture radar. *ISPRS Int. J. Geoinf.* **2018**, *7*, 237. [CrossRef]
32. Schuler, D.L.; Lee, J.-S. Mapping ocean surface features using biogenic slick-fields and SAR polarimetric decomposition techniques. *IEE Proc. Radar Sonar Navig.* **2006**, *153*, 260. [CrossRef]
33. Li, D.; Zhang, Y. Random Similarity Between Two Mixed Scatterers. *IEEE Geosci. Remote Sens. Lett.* **2015**, *12*, 2468–2472.
34. Tong, S.; Liu, X.; Chen, Q.; Zhang, Z.; Xie, G. Multi-feature based ocean oil spill detection for polarimetric SAR data using random forest and the self-similarity parameter. *Remote Sens.* **2019**, *11*, 451. [CrossRef]

35. Peli, E. Contrast in complex images. *J. Opt. Soc. Am. A* **1990**, *7*, 2032–2040. [CrossRef]
36. Yin, J.; Yang, J.; Zhou, Z.; Song, J. The Extended Bragg Scattering Model-Based Method for Ship and Oil-Spill Observation Using Compact Polarimetric SAR. *IEEE J.-Stars* **2015**, *8*, 3760–3772. [CrossRef]

**Disclaimer/Publisher's Note:** The statements, opinions and data contained in all publications are solely those of the individual author(s) and contributor(s) and not of MDPI and/or the editor(s). MDPI and/or the editor(s) disclaim responsibility for any injury to people or property resulting from any ideas, methods, instructions or products referred to in the content.